Simulations and experimental demonstrations of encoding for X-ray coherent scattering

Danae Prokopiou, Kerrie L. Smith, Keith Rogers, Priscila Paula, Paul Evans, Anthony Dicken and Simon Godber

Simulations and experimental demonstrations of encoding for X-ray coherent scattering

Danae Prokopiou,[a]* Kerrie L. Smith,[a] Keith Rogers,[a] Priscila Paula,[a] Paul Evans,[b] Anthony Dicken[b] and Simon Godber[c]

[a]Cranfield Forensic Institute, Cranfield University, Shrivenham SN6 8LA, UK, [b]The Imaging Science Group, Nottingham Trent University, Nottingham NG11 8NS, UK, and [c]HALO X-ray Technologies, Nottingham Trent University, Nottingham NG11 8NS, UK. *Correspondence e-mail: d.prokopiou@cranfield.ac.uk

Diffraction data may be measured using approaches that lead to ambiguity in the interpretation of scattering distributions. Thus, the encoding and decoding of coherent scattering distributions have been considered with a view to enabling unequivocal data interpretation. Two encoding regimes are considered, where encoding occurs between the X-ray source and sample, and where the encoder is placed between the sample and detector. In the first case, the successful recovery of diffraction data formed from the interrogation of powder samples with annular incident beams is presented using a coded aperture approach. In the second regime, encoding of Debye cones is shown to enable recovery of the sample position relative to the detector. The errors associated with both regimes are considered and the advantages of combining the two discussed.

1. Introduction

Signal modulation through coded apertures is a long established approach in X-ray astronomy (Mertz & Young, 1961; Ables, 1968; Dicke, 1968; Skinner, 1984; Busboom *et al.*, 1997) and nuclear medicine (Accorsi *et al.*, 2001; Martineau *et al.*, 2010; Mu *et al.*, 2009) for image recovery. Original applications include, for example, the use of Fresnel zone plates designed to behave as refractive optics within X-ray microscopes (Mertz & Young, 1961; Cannon & Fenimore, 1980). Applications involving the encoding of X-ray diffraction data are uncommon, but recent high-energy studies have shown a significant advantage for such approaches (Faust *et al.*, 2009; Schultz *et al.*, 2009).

Conventionally when applying encoding, the intensity distribution on a detector $P(x, y)$ is formed from the correlation of a coded mask $A(x, y)$ with an object $O(x, y)$. An ideal mask would, in practice, be a pinhole (δ function), but this has limited transmissivity and thus the concept of masks with multiple pinholes was developed (Ables, 1968; Dicke, 1968). A reconstruction or inverse function must be identified that transforms $P(x, y)$ into an accurate representation of $O(x, y)$. Several mask species with various pinhole spatial distributions have been proposed, including random multi-pinhole arrays (Ables, 1968; Dicke, 1968; Cannon & Fenimore, 1980; Weiss *et al.*, 1977; Klotz *et al.*, 1974; Barrett & Swindell, 1981) and uniformly redundant arrays (URAs) (Busboom *et al.*, 1997; Cannon & Fenimore, 1980; Chen & Kishimoto, 2003; Fenimore & Cannon, 1978; Fenimore, 1978; Gottesman & Fenimore, 1989; Ding *et al.*, 2016). URAs can be particularly effective as the autocorrelation of these masks (the system point spread function) approximates a δ function and thus

$$P(x, y) * A(x, y) \simeq O(x, y), \qquad (1)$$

where $*$ denotes the correlation operator.

Previous experimental imaging work has employed encoding masks in pre- or post-object positions (Ignatyev *et al.*, 2011; Olivo *et al.*, 2011). However, such approaches have rarely been employed to encode coherent scattering or aid in the interpretation of X-ray diffraction experiments. A notable exception is work recently reported by Duke University that has sought to encode recoverable information regarding the diffraction source to detector distance of multiple sources along a single axis (MacCabe *et al.*, 2012; Greenberg, Hassan *et al.*, 2014; Greenberg, Krishnamurthy & Brady, 2014; Greenberg *et al.*, 2013). This made elegant use of a simple post-sample comb aperture to encode Debye cones with an intensity modulation having a spatial frequency proportional to the source to detector distance (MacCabe *et al.*, 2012).

Herein, we introduce two unrelated approaches to the application of encoding for diffraction patterns when data are collected in transmission mode. In the first approach, a pre-sample annular mask (that has been shown previously to enhance diffracted intensity relative to a simple pencil beam; Rogers *et al.*, 2010; Evans *et al.*, 2010) results in a scattering distribution that possesses an interpretive ambiguity. We show how this can be resolved using conventional coded aperture decoding algorithms that convolve the captured image with the coded mask (Ables, 1968; Fenimore & Cannon, 1978; Ballesteros *et al.*, 1996; Chen & Kishimoto, 2003). In the second approach (solving a different problem), we use post-sample encoders to determine the unknown position of either single or multiple diffraction sources and explore the precision with which this can be achieved.

Both coded aperture approaches introduced by this work have applications in areas where high-speed identification is required, in particular where the sample's position within a volume is unknown. For example, materials discrimination within the aviation security sector is relatively poor; thus the techniques could be exploited to identifying illicit materials within luggage.

2. Experimental

2.1. Pre-sample encoding

The use of annular coded masks was examined some years ago for enhanced nuclear medicine imaging (Walton, 1973; Simpson, 1978). More recently, annular incident beam masks have been shown to provide a novel geometry within diffraction experiments that produce unique high-intensity maxima (corresponding to Bragg peaks) along a single axis (Rogers *et al.*, 2010; Evans *et al.*, 2010). An annular beam also has the advantage for some applications of utilizing a greater cross section of the interrogating sample area when compared to traditional X-ray diffraction beams. This is important for applications such as security screening, requiring simultaneous integration of a large volume, as well as when dealing with samples exhibiting some preferred orientation or large grain size (Chan *et al.*, 2010; Evans *et al.*, 2010; Rogers *et al.*, 2012).

The scattering distribution measured in a plane parallel to the coded aperture consists of concentric 'rings' of high intensity formed from a superposition of multiple Debye cones. Unfortunately, the ring caustics are formed from both diverging and converging scattering cones and are thus difficult to interpret; for example, d spacings cannot be directly calculated from the detector images unless scanning is applied. However, application of a traditional coded aperture approach is able to solve this problem. Consider a circular δ function that is zero except at points on a circle of radius c, *i.e.* $\delta(r - c)$. The autocorrelation of this function is given by

$$\int_0^\infty \left[\delta(r_0 - c)\delta(|\mathbf{r} - \mathbf{r}_0|) - c \right] \mathrm{d}^2 r_0 = \frac{4c^2}{r(4c^2 - r^2)^{1/2}}, \qquad (2)$$

where $\mathbf{r}$ and $\mathbf{r}_0$ are two-dimensional vectors with Cartesian coordinates (x, y) and (x_0, y_0), respectively, and $|\mathbf{r}| = r$ (Barrett & Swindell, 1981). This has a relatively high intensity central maximum and a low intensity distribution in the range $0 < x < 2c$ and thus approximates a δ function, albeit with side lobes.

The relationship presented in equation (1) was applied to the scattering distributions from a specimen by regarding the Debye cones as the 'object' to be recovered [$O(x, y)$] through convolution with the annular function [$A(x, y)$]. This method assumes that the material under examination is distributed homogeneously over the annular footprint of the incident beam and is experimentally illustrated within Fig. 1.

A simulation was used to illustrate the principle and develop the processing protocol. This involved convolving single images with an image of the primary beam captured at the sample's position. A bandpass filter (filtering large structures down to 40 pixels and small structures up to 3 pixels) and thresholding (dc level removal) was then applied to the resulting image using the *ImageJ* software (Schneider *et al.*, 2012). Further explanation and details on this process were reported by Prokopiou (2014). This protocol was subsequently followed using experimental data obtained with Zr-filtered molybdenum radiation, an annular collimator (17.5 and 18 mm inner and outer diameters, respectively) at 140 mm from the X-ray source, a $\sim$0.2 mm thick aluminium oxide (Al_2O_3) sample at $\sim$150 mm and a PIXIS 1024 (two-
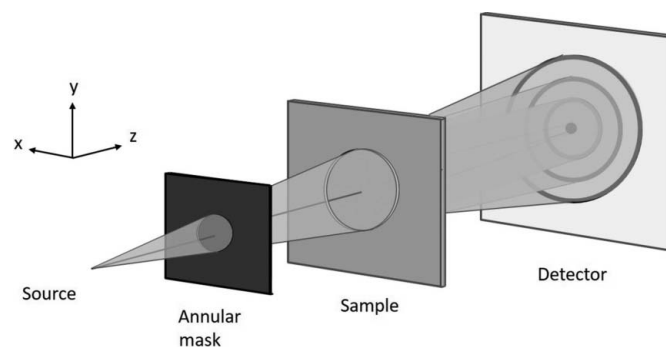

Figure 1
The experimental arrangement for the pre-sample encoding using an annular mask.

dimensional Gadox – Princeton Instruments) 13.3 × 13.3 mm area CCD detector with 1024 × 1024 pixels at 15 mm from the sample.

2.2. Post-sample encoding

In addition to the coded aperture (CA) treatment in §2.1 used to recover the diffraction data, we have also employed simple post-sample encoding to determine unknown diffraction source positions. In this case, using simple transmission geometry, an encoder is placed between the sample and detector plane to completely absorb relatively small areas of the scattering distributions (see Fig. 2). We explored the use of two novel encoders (linear and Archimedean spiral), each with a high open fraction of ∼90%. We have demonstrated the ability of these post-sample encoders to unambiguously encode conventional pencil beam diffraction data. The linear encoder was employed because of its simplicity, whereas the spiral was used to overcome potential limitations of the linear case (see §3.2.1).
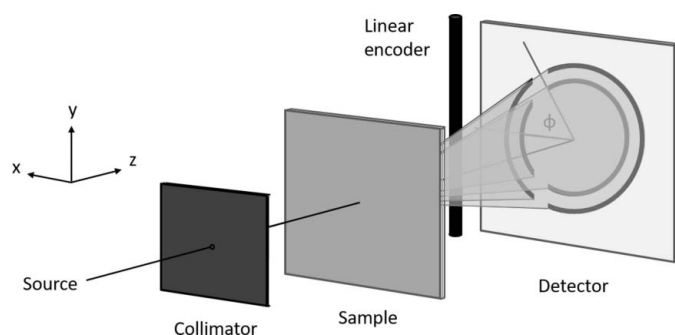

Figure 2
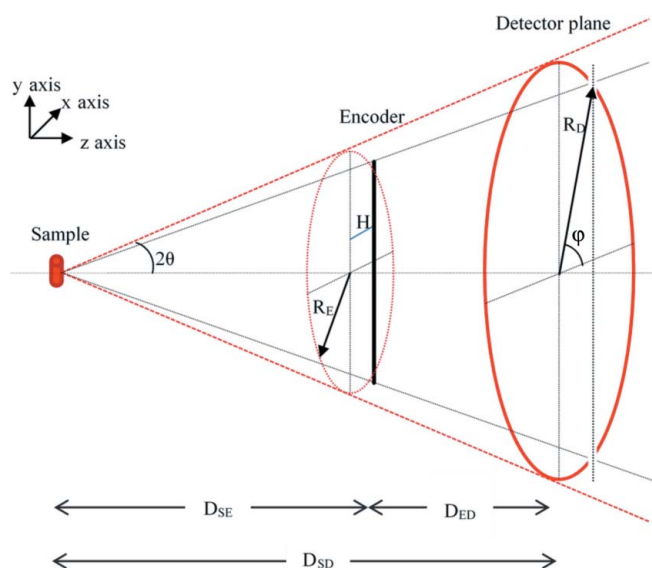The experimental arrangement for the post-sample encoding using a simple linear encoder.

Figure 3
The geometric arrangement employed to record the two-dimensional X-ray diffraction data encoded by a single post-sample encoder (in this example a linear encoder), when illuminated by a pencil beam.

In both cases the sample to detector distance (D_{SD}) and Bragg angle of each diffraction maximum (θ) were determined independently using

$$D_{SD} = D_{ED}\left[1 + \left(\frac{R_E}{R_D - R_E}\right)\right], \quad (3)$$

$$2\theta = \tan^{-1}\left(\frac{R_D - R_E}{D_{ED}}\right), \quad (4)$$

where D_{ED} is the encoder to detector distance, and R_D and R_E are the radii of an arbitrary Debye ring at the detector plane and encoder plane, respectively (see Fig. 3). R_E may be determined for the linear encoder from $R_E = H/\cos\varphi$ and for the spiral encoder from $R_E = a + b\varphi$, where H is the encoder's lateral position relative to the primary X-ray beam, a and b are characteristics of the spiral, and φ is the azimuthal angle of encoding obscuration relative to the horizontal plane. The variables D_{ED}, H, a and b are fixed by the experiment, and therefore measurement of φ and R_D for each Debye ring enables determination of D_{SD} and 2θ.

Initially, simulations were performed with *McXtrace* (Bergback Knudsen *et al.*, 2013) to examine various encoder geometries and forms. An error study was undertaken to explore how experimental uncertainties (*e.g.* encoder to detector distance) would propagate to estimations of sample position (distance D_{SD}) and 2θ.

Subsequently, experimental data were collected with a simple pencil beam transmission arrangement (Cu *Kα*) and a GADDS (General Area Detector Diffraction System, supplied by Bruker) area detector. The encoders were formed from 0.5 mm diameter tungsten wire, and the spiral was constructed as a simple single turn to avoid potential ambiguity arising from multiple encoding.

3. Results and discussion

3.1. Pre-sample encoding

Fig. 4(*a*) illustrates a typical scattering distribution from an angular dispersive experiment in which a thin (∼0.2 mm) plate of Al_2O_3 was illuminated with a pencil beam. The relatively small detector active area required 5 × 5 tiling in order to measure a minimum *d* spacing of ∼0.15 nm at the detector distance employed. The horizontal obscured rectangular area artefact was a result of limited *x/y* positioning of the sample stage. Fig. 4(*b*) shows a typical scattering pattern produced when using the pre-sample annular encoding mask. The apparent concentric rings should not be confused with the Debye rings observed during a pencil beam and flat detector conventional Laue type experiment; the central high-intensity maximum shown in Fig. 4(*b*) is not the main interrogating X-ray beam. For further details on the geometrical origin of the concentric rings illustrated in Fig. 4(*b*) the reader should refer to Fig. 1 of Evans *et al.* (2010).

This central high intensity results from the condition that (annular radius)/(Debye cone radius) ≃ 1 for a particular set of diffracting planes. For this condition to be met, the sample
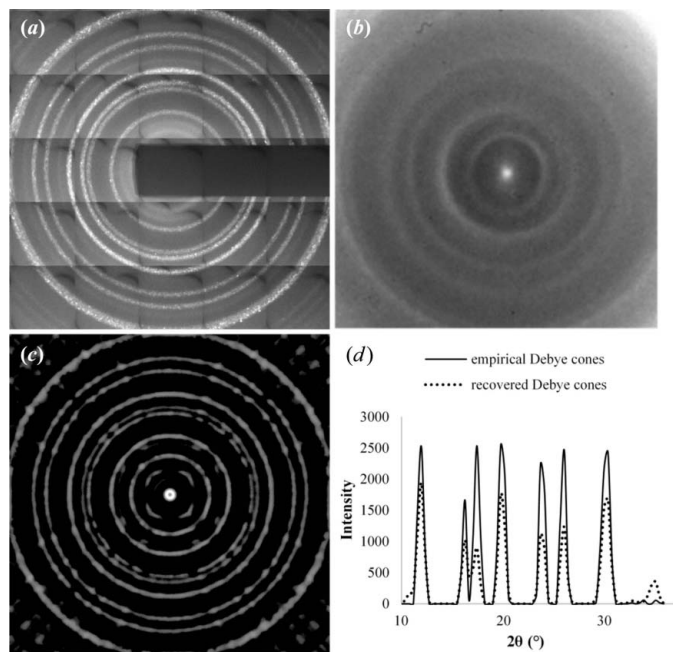
Figure 4
Experimental results of coded aperture processing. (*a*) Conventional pencil beam transmission diffraction data from a ∼0.2 mm thick Al_2O_3 plate, (*b*) observed diffraction pattern from a ∼0.2 mm thick Al_2O_3 plate with an annular pre-sample aperture, (*c*) recovered Debye rings following convolution of (*b*) with a captured image of the incident annular beam at the sample's *z* position, and (*d*) radial integration of (*a*) and (*c*).

(or detector) is translated along the primary beam axis until annular radius = Debye cone radius (Rogers *et al.*, 2010). However, the CA approach presented herein does not require this condition. For the purpose of this study, a mask incorporating an annular transparent region was employed as the coded aperture. As indicated by equation (2) and shown in Fig. 5, the autocorrelation of the annular mask approximates a δ function with side lobes. Hence, an annular mask was convolved with the primary data collected at the detector. Fig. 4(*c*) shows the result of this convolution following the application of a bandpass filter and thresholding. Comparing this result with that from the pencil beam experiment shows that, at least qualitatively, the Debye cones have been accurately recovered. This was further demonstrated by a comparison of the diffractograms (see Fig. 4*d*) derived from the radial integration of data presented in Figs. 4(*a*) and 4(*c*). The position of each diffraction peak's maximum intensity was obtained and compared with the corresponding peak in the recovered data *via* a residual sum of squares (RSS) analysis. The resulting RSS value was $0.02°$ (2θ), indicating a strong agreement between conventional dif-

fraction data and recovered Debye cones in terms of peak positions. The source of discrepancies between relative intensities is due to (i) different sampling volumes and therefore different preferred orientations, and (ii) differences in Lorentz factors.

3.2. Post-sample encoding

3.2.1. Linear encoder simulation. Simulations were conducted with calcite ($CaCO_3$) samples of thickness 0.05 mm illuminated with a pencil beam (Cu $K\alpha$ radiation). Calcite was chosen as the diffraction data have a dominant diffraction maximum from the 104 reflection (thus enabling some clarity) and 0.05 mm allowed sufficient transmission to observe diffraction from multiple samples simultaneously. The offset distance of the linear encoder, H, and encoder to detector distance, D_{ED}, were systematically changed and coherent scattering distributions calculated at each point. The magnitude of the errors when determining the sample to detector distance (D_{SD}) from the inner 104 Debye cone was calculated *via* analytical error propagation and the results are shown in Fig. 6(*a*). This demonstrates that the position of the linear encoder for minimizing errors in estimated sample position occurs when the encoder to incident beam distance, H, is greatest and the encoder is positioned close to the sample, *i.e.* the distance between the linear encoder and detector, D_{ED}, is maximized. This is only true when the linear encoder interrupts the Debye cone, *i.e.* H is limited by the radius of the Debye cone at distance D_{ED}.

The same trend can be observed when calculating the associated error of the scattering angle, 2θ, at each linear encoder location (Fig. 6*b*). Thus, errors in the determination of 2θ and sample position are minimized when D_{ED} and H are maximized, with the limitation that the encoder must still interrupt the Debye cone. The most dominant source of error
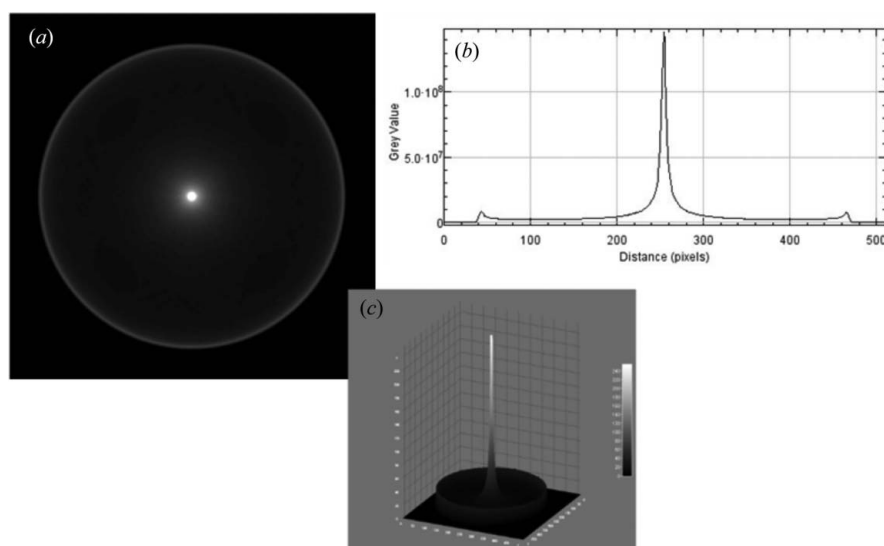

Figure 5
(*a*) Two-dimensional image of the autocorrelation of an annular aperture, (*b*) two-dimensional profile plot of (*a*), and (*c*) three-dimensional surface plot of (*a*).
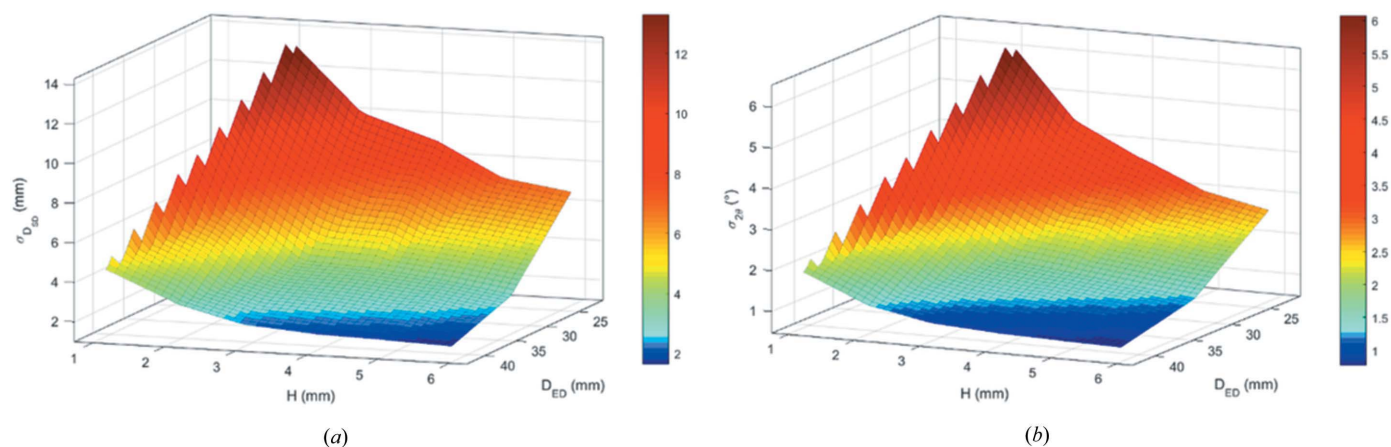
Figure 6
(*a*) Three-dimensional surface plot of sample to detector distance error and (*b*) three-dimensional surface plot of error associated with measuring the scattering angle (2θ) calculated using the 104 reflection from the sample closest to the detector with a linear post-sample encoder.

for these experimental conditions, with a 1% error in all variables, was associated with D_{ED}, the distance between the linear encoder and detector.

3.2.2. Linear encoder experimental. Initially, a sample of Al_2O_3 (plate) was placed at a known distance from the detector and the subsequent two-dimensional scattering data were used to calibrate critical encoder parameters, such as the encoder to detector distance (D_{ED}) and the encoder's lateral position relative to the primary X-ray beam (H). A series of experiments were then performed by collecting scattering data as the sample to detector distance was changed to confirm that the encoding behaved as predicted by equations (3) and (4) and the simulation.

The result from a multiplex sampling (>1 sample spatially separated along the primary axis) experiment is shown in Fig. 7(*a*). Here, two thin samples (~0.05 mm) of calcite-loaded cellulose were simultaneously placed within the primary beam at different distances from the detector. The scattering distribution is therefore the weighted sum of diffraction patterns from both samples. The occluded sections created by the encoder are clearly visible as vertical obscured regions, and the encoding positions can be quantified from azimuthal plots such as those shown in Fig. 7(*b*) for the 104 calcite maxima corresponding to each sample.

Subsequent application of equations (3) and (4) is shown in Table 1, where the *d* spacing and sample to detector distances are seen to be the same as their known values, within experimental errors. Thus, the position and *d* spacing(s) (and therefore material phase) can, in principle, be determined with no *a priori* knowledge of the object position.

3.2.3. Archimedean spiral encoder simulation. Simulations were also conducted with an Archimedean spiral encoder and two calcite samples of thickness 0.05 mm, spatially separated along the primary beam axis. To illustrate the effectiveness of the approach, one of the plates was held stationary while the other was translated in 2 mm steps along the primary X-ray beam towards the stationary detector. The
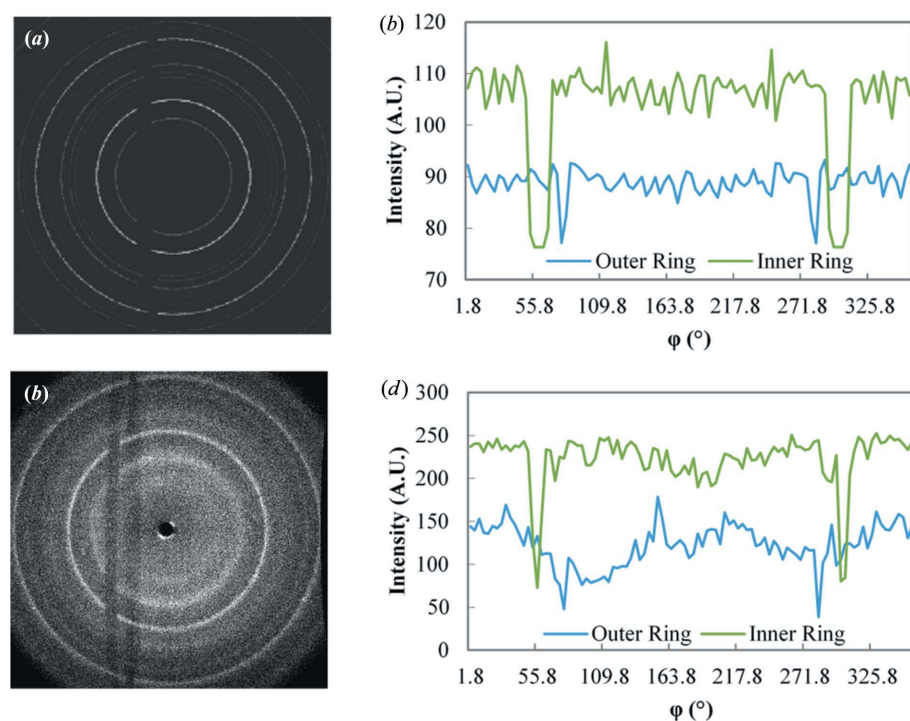

Figure 7
(*a*) Simulated image obtained with an off-centre linear encoder (H = 6 mm, D_{ED} = 37 mm) with two 0.05 mm thick calcite samples separated by 32 mm along the primary beam axis. The two brightest rings, from different calcite samples, have radii of 30 and 54 mm. (*b*) Azimuthal plots of simulated data (*a*) showing the encoding position for each high-intensity Debye ring. (*c*) Diffraction pattern from a pair of calcite samples under the same experimental configuration as the simulations. (*d*) Azimuthal plots of experimental data (*c*).

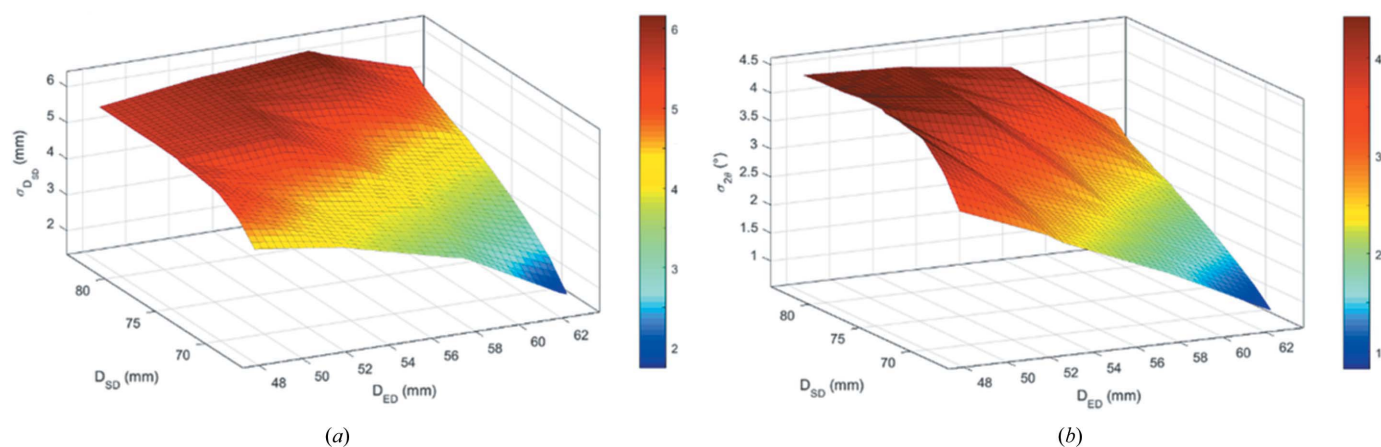Danae Prokopiou *et al.* · Encoding for X-ray coherent scattering **415**

Figure 8
(a) Three-dimensional surface plot of sample to detector distance error and (b) three-dimensional surface plot of error associated with measuring the scattering angle (2θ) calculated using the 104 calcite maxima from the sample closest to the detector with an Archimedean post-sample encoder.

errors associated with determination of the sample to detector distance (D_{SD}) and 2θ (from the 104 Debye cone) are shown in Figs. 8(a) and 8(b), respectively.

As with the linear encoder, the position that minimizes errors in scattering angle and sample position occurs when the spiral is closest to the sample, *i.e.* when D_{ED} is maximized. The

Figure 9
(a) A sequence of simulated images and (b) a sequence of diffraction patterns from of a pair of calcite samples spatially separated along the primary axis with a spiral encoder in front of the detector. The sequence was recorded as one of the samples was translated in 2 mm steps towards the detector face.

error in the calculated sample relative position was dominated by the measurement error in the encoder to detector distance. For the calculated scattering angle, 2θ, the greatest contribution to the total error was from the measurement error in the Debye ring radius.

3.2.4. Archimedean spiral encoder experimental. Several experiments were performed, including changing the sample to detector distance for a single sample and for multiple samples. To illustrate the encoding, Fig. 9 shows a sequence of scattering patterns collected from the two plate samples of calcite. The Debye cone encoding is apparent as limited opaque regions within each Debye ring. Using the dominant 104 scattering maxima, it is apparent that the encoding region associated with the translating sample appears to rotate simultaneously with a decrease in the associated Debye ring radius.

The radii of the Debye rings and their encoding φ angles were measured, and the scattering angles and sample to detector distances calculated at each translation step. The data are presented in Table 2, which indicates a good agreement with the expected results for both parameters.

An analytical error analysis of these post-sample encoder geometries shows that the parameters with the most significant influence on estimated sample to detector distance and scattering angle are the encoder to detector distance and measured Debye ring radius, respectively.

For the linear encoder, a large wire to primary axis distance increases precision, but unfortunately this coincides with a less accurate determination of φ and a limited d-spacing range.
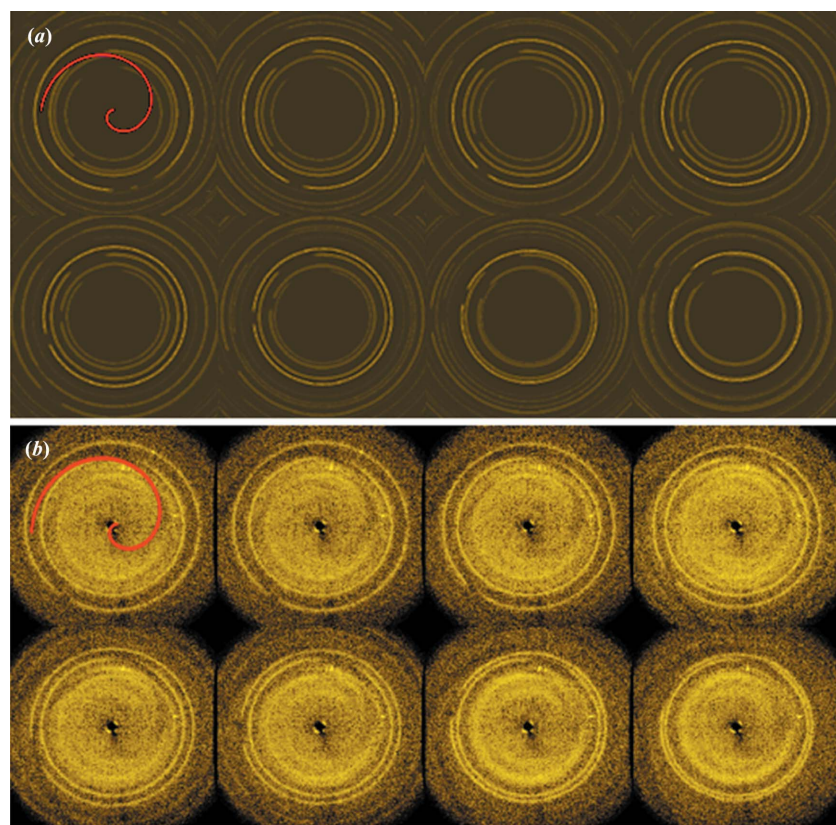
Table 1
Results of the linear encoding recovery.

Samples 1 and 2 were placed at 60 and 92 mm, respectively, from the detector. The corresponding d spacings for cellulose and calcite are 0.39002 and 0.3035 nm, respectively (ICDD database PDF 50-2241 and PDF 5-586).

Debye ring source	R_D (mm)	φ (°)	Calculated sample to detector distance (mm)	Calculated d spacing (nm)
Sample 1: cellulose	25	47	59.9 (7)	0.39 (2)
Sample 1: calcite	34	59	59.6 (6)	0.30 (2)
Sample 2: cellulose	39	75	93.0 (6)	0.39 (2)
Sample 2: calcite	52	78	91.1 (6)	0.30 (2)

Table 2
Results of the spiral encoding recovery.

Sample 1 remained stationary while the sample to detector distance was incrementally increased for sample 2. The corresponding d spacing for the 104 reflection of calcite is 0.3035 nm (ICDD database PDF 5-586).

Debye ring source	R_D (mm)	φ (°)	R_E (mm)	Calculated d spacing (nm)	Calculated sample to detector distance (mm)	Measured sample to detector distance (mm)
Sample 1: fixed	37	165	6.7	0.30 (4)	66.0 (5)	67
Sample 2: step 0	46	312	15.8	0.30 (3)	82.6 (5)	83
Sample 2: step 1	45	304	15.2	0.31 (3)	81.6 (5)	81
Sample 2: step 2	44	289	14.1	0.31 (3)	79.6 (5)	79
Sample 2: step 3	42	268	12.6	0.31 (3)	76.8 (5)	77
Sample 2: step 4	41	254	11.6	0.31 (3)	75.1 (5)	75
Sample 2: step 5	40	234	10.4	0.30 (3)	72.8 (5)	73
Sample 2: step 6	39	218	9.4	0.30 (3)	71.0 (5)	71

4. Conclusions

Two different methods for encoding angular dispersive, transmission diffraction data have been presented. We have shown how, by adopting a conventional coded aperture reconstruction process, conventional scattering distributions (*i.e.* Debye cones) may be recovered from the scattering patterns produced from an annular pre-sample aperture. We have also shown how sample position and material phase information may be recovered through post-sample encoding. An application area which can benefit from both methods is detection of threat materials or illicit drugs in luggage or parcels. The approach is currently the subject of study for employment within baggage screening systems.

The pre-sample annular coded aperture geometry was shown to produce a scattering pattern with several notable features. High-intensity 'condensation' points at the centre of the patterns occur when the Debye cone radius and mask annular radius are equal. Interestingly perhaps, at sample positions where this condition is not true, in principle, there is no coherent scattering contribution at the diffraction pattern centre. Unfortunately, these scattering patterns are difficult to interpret; radial integration produces diffractograms with two overlapping d-spacing scales owing to the converging and diverging nature of the Debye cones. However, we have shown that these scattering patterns can be interpreted through convolution with the annular mask as a result of the near singular feature of the mask autocorrelation function. It

can also be anticipated that using a mask annulus with a radius significantly greater than that of the Debye cones would produce an improved convolution reconstruction as the lobe extremes in the autocorrelation function (shown in Fig. 5) would contribute less to the final result. This is because the lobe extremes present in the annulus' autocorrelation function are the only source of reconstruction 'confusion', *i.e.* the only deviation from an ideal δ function (see Fig. 5). We continued the simulation studies and the results indicated that recovery was also effective with poorer signal to noise ratio (in the measured data) or geometric distortion of the annular mask. However, the ambiguity in the Debye cones produced by this geometry means that the post-sample encoding solution demonstrated by Duke would be ineffective for these data (see below) (MacCabe *et al.*, 2012).

The second encoding approach introduced in this study, linear and spiral post-sample encoders, was shown to be effective at providing geometric and structural information. Material phase identification (through d-spacing determination) can be achieved with no *a priori* knowledge of the sample's position relative to the detector. Linear and spiral encoders were shown to provide single axis positions with ~1% precision, although accurate calibration was essential, especially with the spiral encoder where small manufacturing errors (affecting a and b) significantly influence the derived parameters. Comparison of the induced errors from both encoders with 1% error in all their variables indicated that the Archimedean spiral yields a lower experimental error in the calculated D_{SD} distance (~7.5 times lower) than the linear encoder.

We anticipate that the combination of an incident beam annular mask and post-sample linear encoder has advantages over alternative coded aperture approaches. For example, a linear encoder (such as that described above) would provide sample position information, overcoming the inherent ambiguity in the converging and diverging Debye cones generated by conventional post-sample encoders. The convergence point acts as an inversion centre, thus enabling discrimination between a converging and diverging Debye cone. Furthermore, such simple encoders have a high open fraction compared to conventional coded apertures and thus maximize the number of measured photons at the detector.

References

Ables, J. G. (1968). *Publ. Astron. Soc. Aust.* **1**, 172–173.
Accorsi, R., Gasparini, F. & Lanza, R. C. (2001). *Nucl. Instrum. Methods Phys. Res. Sect. A*, **474**, 273–284.
Ballesteros, F. J., Sanchez, F., Reglero, V., Porras, E., Perez, F. & Robert, A. (1996). *Proceedings, 2nd INTEGRAL Workshop 'The Transparent Universe'*, pp. 357–360. Noordwijk: ESA Publications Division.
Barrett, H. H. & Swindell, W. (1981). *Radiological Imaging: The Theory of Image Formation, Detection, and Processing*. New York: Acasemic Press.
Bergbäck Knudsen, E. *et al.* (2013). *J. Appl. Cryst.* **46**, 679–696.

Busboom, A., Schotten, H. D. & Elders-Boll, H. (1997). *J. Opt. Soc. Am. A*, **14**, 1058–1065.

Cannon, T. M. & Fenimore, E. E. (1980). *Opt. Eng.* **19**, 283–289.

Chan, J., Evans, P., Wang, X., Godber, S., Peatfield, I., Rogers, K., Rogers, J. & Dicken, A. (2010). *44th Annual 2010 IEEE International Carnahan Conference on Security Technology*, pp. 142–147. IEEE.

Chen, Y. W. & Kishimoto, K. (2003). *Rev. Sci. Instrum.* **74**, 2232–2235.

Dicke, R. H. (1968). *Astrophys. J.* **153**, L101–L105.

Ding, J., Noshad, M. & Tarokh, V. (2016). *J. Opt. Soc. Am. A*, **33**, 863–881.

Evans, P., Rogers, K., Chan, J., Rogers, J. & Dicken, A. (2010). *Appl. Phys. Lett.* **97**, 204101.

Faust, A. A., Rothschild, R. E., Leblanc, P. & McFee, J. E. (2009). *IEEE Trans. Nucl. Sci.* **56**, 299–307.

Fenimore, E. E. (1978). *Appl. Opt.* **17**, 3562–3570.

Fenimore, E. E. & Cannon, T. M. (1978). *Appl. Opt.* **17**, 337–347.

Gottesman, S. R. & Fenimore, E. E. (1989). *Appl. Opt.* **28**, 4344–4352.

Greenberg, J. A., Hassan, M., Krishnamurthy, K. & Brady, D. (2014). *Analyst*, **139**, 709–713.

Greenberg, J., Krishnamurthy, K. & Brady, D. (2014). *Opt. Lett.* **39**, 111–114.

Greenberg, J. A., Krishnamurthy, K., Lakshmanan, M., MacCabe, K., Wolter, S., Kapadia, A. & Brady, D. (2013). *Proc. SPIE*, **8858**, 885813.

Ignatyev, K., Munro, P. R. T., Speller, R. D., Olivo, A., McNulty, I., Eyberger, C. & Lai, B. (2011). *AIP Conf. Proc.* **1365**, 254–257.

Klotz, E., Linde, R. & Weiss, H. (1974). *Opt. Commun.* **12**, 183–187.

MacCabe, K., Krishnamurthy, K., Chawla, A., Marks, D., Samei, E. & Brady, D. (2012). *Opt. Express*, **20**, 16310–16320.

Martineau, A., Rocchisani, J. M. & Moretti, J. L. (2010). *Nucl. Instrum. Methods Phys. Res. Sect. A*, **616**, 75–80.

Mertz, L. & Young, N. O. (1961). *Proceeding of the International Conference on Optical Instruments and Techniques*, pp. 305–310. London: Chapman and Hall.

Mu, Z., Hong, B., Li, S. & Liu, Y. H. (2009). *Med. Phys.* **36**, 1533–1542.

Olivo, A., Ignatyev, K., Munro, P. R. T. & Speller, R. D. (2011). *Nucl. Instrum. Methods Phys. Res. Sect. A*, **648**, S28–S31.

Prokopiou, D. (2014). PhD thesis, Cranfield University, Shrivenham, UK.

Rogers, K., Evans, P., Prokopiou, D., Dicken, A., Godber, S. & Rogers, J. (2012). *Nucl. Instrum. Methods Phys. Res. Sect. A*, **690**, 1–6.

Rogers, K., Evans, P., Rogers, J., Chan, J. & Dicken, A. (2010). *J. Appl. Cryst.* **43**, 264–268.

Schneider, C. A., Rasband, W. S. & Eliceiri, K. W. (2012). *Nat. Methods*, **9**, 671–675.

Schultz, L. J. *et al.* (2009). *Nucl. Instrum. Methods Phys. Res. Sect. A*, **608**, 267–274.

Simpson, R. G. (1978). PhD thesis, The University of Arizona, Tucson, Arizona, USA.

Skinner, G. K. (1984). *Nucl. Instrum. Methods Phys. Res.* **221**, 33–40.

Walton, P. W. (1973). *J. Nucl. Med.* **14**, 861–863.

Weiss, H., Klotz, E., Linde, R., Rabe, G. & Tiemens, U. (1977). *Opt. Acta Int. J. Opt.* **24**, 305–325.